

## Nonlinear corner states in a topologically nontrivial kagome lattice

K. Prabith<sup>1</sup>, Georgios Theocharis<sup>2</sup>, and Rajesh Chaunsali<sup>1,\*</sup>

<sup>1</sup>Department of Aerospace Engineering, Indian Institute of Science, Bangalore 560012, India

<sup>2</sup>LAUM, CNRS-UMR 6613, Le Mans Université, Avenue Olivier Messiaen, 72085 Le Mans, France



(Received 31 March 2024; revised 24 June 2024; accepted 13 September 2024; published 24 September 2024)

We investigate a higher-order topological insulator (HOTI) under strong nonlinearity, focusing on the existence and stability of high-amplitude corner states, which can find applications in optics, acoustics, elastodynamics, and other wave-based systems. Our study centers on a breathing kagome lattice composed of point masses and springs, known to exhibit edge and corner states in its linear regime. By introducing on-site cubic nonlinearity, we analyze its impact on both edge and corner states. The nonlinear continuation of the corner state unveils stable high-amplitude corner states within the lattice, featuring nonzero displacements at even sites from the corner—a characteristic absent in the linear limit. Interestingly, the nonlinear continuation of the edge state reveals its transformation into distinct families of high-amplitude corner states via two pitchfork bifurcations. While some states maintain stability, others become unstable through real instability and Neimark-Sacker bifurcation. These unstable corner states dissipate their energy into the edges and the bulk over an extended period, as corroborated by long-time dynamical simulations. Consequently, our study provides insights into achieving significant energy localization at the corners of HOTIs through various classes of nonlinear states.

DOI: [10.1103/PhysRevB.110.104307](https://doi.org/10.1103/PhysRevB.110.104307)

### I. INTRODUCTION

In recent years, higher-order topological insulators (HOTIs) have emerged as a novel category of topological materials, distinguished by the emergence of topologically protected, gapless states localized at the corners or hinges of 2D and 3D lattices [1–5]. Initially, this class included second-order topological quadrupole insulators featuring nonzero quadrupole moments, necessitating negative hopping. However, an alternative approach, rooted in nonzero bulk dipole moments and exploiting crystalline symmetry, has been proposed to realize second-order topological insulators [6]. This method utilizes the “filling anomaly” to establish the presence of higher-order states. The exploration of HOTIs has yielded a myriad of examples in both classical and quantum domains, sparking innovations in photonics [7,8], plasmonics [9], phononics [10,11], magnets [12], stochastic systems [13], and circuit design [14,15] (see also the review by Xie *et al.* [16] and references therein). Therefore, HOTIs can find applications in constructing advanced acoustic and energy-harvesting devices, corner-mode lasers, topoelectrical circuits, thermal management systems, and more.

The entire framework of higher-order topology rests on the linear dynamics of the lattice. Exploring the interplay between nonlinearity and higher-order topology is one of the emerging research questions. Recently, this interplay has been investigated in the context of conventional (not higher-order) topological systems, revealing several intriguing phenomena [17]. For example, nonlinearity has been utilized to tune the existence and stability of topological edge and interface states [18–33] and to generate harmonics [34–36]. Furthermore, insights from topological band theory have revealed

special characteristics of bulk solitons and breathers [37–40]. Nonlinear bulk solutions have also been used to interpret nonlinear edge solutions [41,42]. Moreover, local topological invariants have been used for deciphering topological phenomena in nonlinear systems [43–45]. Finally, through some special types of nonlinearities, “self-induced” boundary states [46–52] and domain walls [53–56] have been observed. However, there are very limited studies on nonlinear HOTIs [57–63]. In particular, the existence and stability of different classes of high-order topological states in strongly nonlinear lattices remain unexplored.

In this study, we investigate a breathing kagome lattice composed of point masses and springs, which exhibits on-site cubic nonlinearity. This model, described by second-order ordinary differential equations, is a universal model applicable not only in mechanical systems [64] but also in optical [65,66], electrical [67], and superconducting circuits [68]. On-site nonlinearity in mechanical settings is common due to geometric nonlinearity [69], while in optical and superconducting (Josephson-junctions) settings, it arises due to the Kerr effect [70] and magnetic flux [69], respectively. While kagome lattices have been previously explored for bulk nonlinear breathers [71–74], recent studies have revealed the presence of higher-order topological states at the corners of kagome lattices, resulting from topological transitions [75–81]. Our focus is on probing the existence and stability of highly nonlinear states localized at the corners of the lattice. We employ a nonlinear continuation technique on topological corner states to derive a family of high-amplitude corner states. Furthermore, considering that the kagome lattice also supports edge states, we utilize a nonlinear continuation technique on these states to unveil an entirely new family of high-amplitude corner states, as depicted by detailed bifurcation diagrams.

\*Contact author: rchaunsali@iisc.ac.in

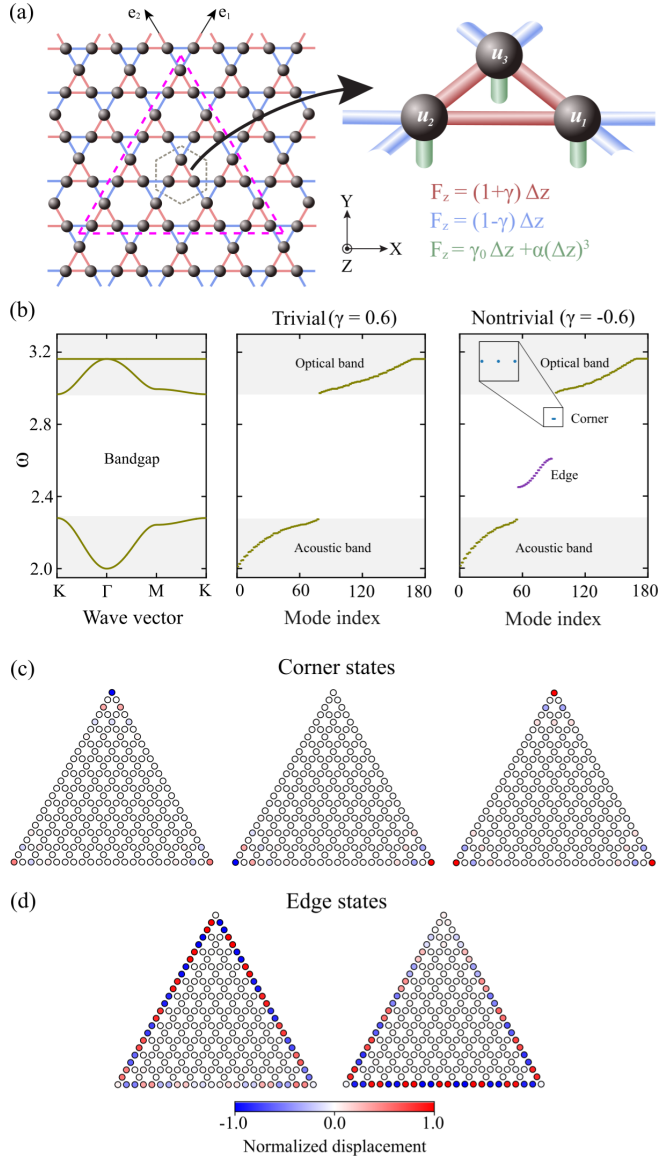


FIG. 1. Nonlinear kagome lattice and its linear characteristics. (a) Schematic of a kagome lattice composed of point masses connected by linear springs (red and blue) and grounded with nonlinear spring (green). The inset displays the unit cell in 3D. The expressions for the force ( $F_z$ ) with respect to the deformation ( $\Delta z$ ) are indicated using different colors. (b) Dispersion diagram and eigenspectra of the finite triangular lattice (shown by the pink dashed line) under trivial ( $\gamma = 0.6$ ) and nontrivial ( $\gamma = -0.6$ ) conditions. Corner and edge states are highlighted inside the band gap. (c), (d) Profiles of corner and edge states, respectively. The color bar denotes the out-of-plane displacements of the masses on a scale from  $-1$  to  $1$ , normalized with respect to the maximum amplitude.

## II. SYSTEM AND ITS LINEAR DYNAMICS

We investigate an infinite kagome lattice composed of point masses and springs, as illustrated in Fig. 1(a). The unit cell (inset) comprises three masses connected by intracell stiffness  $k_1$  (highlighted in red) and intercell stiffness  $k_2$  (highlighted in blue), where  $k_1 = k(1 + \gamma)$  and  $k_2 = k(1 - \gamma)$ , with  $\gamma \in (-1, 1)$ . The scalar  $\gamma$ , termed the stiffness differen-

tial, determines the mismatch between intracell and intercell stiffnesses. The masses are secured via a grounded spring (depicted in green), characterized by linear stiffness  $k_0$  and nonlinear stiffness  $k_{nl}$  introducing cubic nonlinearity. We consider one degree of freedom per particle, which could potentially represent either out-of-plane motion (transverse vibrations) in a lattice of masses [82] or rotations in a lattice of spinners [23,83]. For convenience, the nondimensionalized equations of motion for the masses within the unit cell, neglecting any dissipative effects, are expressed as follows:

$$\begin{aligned} \ddot{u}_{1,m,n} + (1 + \gamma)(2u_{1,m,n} - u_{2,m,n} - u_{3,m,n}) + \gamma_0 u_{1,m,n} + \alpha u_{1,m,n}^3 \\ + (1 - \gamma)(2u_{1,m,n} - u_{2,m+1,n-1} - u_{3,m-1,n}) = 0, \\ \ddot{u}_{2,m,n} + (1 + \gamma)(2u_{2,m,n} - u_{3,m,n} - u_{1,m,n}) + \gamma_0 u_{2,m,n} + \alpha u_{2,m,n}^3 \\ + (1 - \gamma)(2u_{2,m,n} - u_{3,m-1,n} - u_{1,m-1,n+1}) = 0, \\ \ddot{u}_{3,m,n} + (1 + \gamma)(2u_{3,m,n} - u_{1,m,n} - u_{2,m,n}) + \gamma_0 u_{3,m,n} + \alpha u_{3,m,n}^3 \\ + (1 - \gamma)(2u_{3,m,n} - u_{1,m,n+1} - u_{2,m+1,n}) = 0, \end{aligned} \quad (1)$$

where the variables  $u_{1,m,n}$ ,  $u_{2,m,n}$ , and  $u_{3,m,n}$  represent the nondimensionalized out-of-plane displacements of the three masses with respect to a reference length  $a$ . The indices  $m$  and  $n$  indicate the unit cell's position along its two basis vectors,  $e_1$  and  $e_2$ , as depicted in Fig. 1(a). Overdots denote derivatives with respect to nondimensionalized time.  $\gamma_0$  and  $\alpha$  are the nondimensionalized parameters such that  $\gamma_0 = k_0/k$  and  $\alpha = a^2 k_{nl}/k$  (see Ref. [48] for more details).

In the linear limit ( $\alpha \rightarrow 0$ ), assuming a harmonic plane-wave solution, we obtain the dispersion diagram for the parameters  $\gamma = \pm 0.6$  and  $\gamma_0 = 4$ , as depicted in Fig. 1(b). It consists of two dispersive bands—the acoustic band and the optical band—as well as a flat band. The flat band touches the optical band at the  $\Gamma$  point. For a nonzero stiffness differential, a band gap exists between the acoustic and optical bands and the system is a *nontrivial* HOTI for  $\gamma < -1/3$  [75,76]. It can support higher-order topological states inside the band gap for finite lattices with triangular or parallelogram shapes. In this analysis, we employ a finite kagome lattice of triangular shape, cut from the infinite lattice [pink dashed triangle in Fig. 1(a)] with its boundaries fixed. The eigenspectra of the lattice, consisting of 78 unit cells, are presented for both the *nontrivial* case ( $\gamma = -0.6$ ) and the *trivial* case ( $\gamma = 0.6$ ) in Fig. 1(b) (refer to Appendix A for the evolution of the spectrum as the stiffness differential  $\gamma$  is varied). In the *trivial* lattice, no states exist within the band gap, while in the *nontrivial* case, multiple states are observed within the band gap. These states are localized either at the edges or at the corners of the finite lattice, referred to as “edge states” and “corner states,” respectively, throughout the remainder of the manuscript.

The corner states are nearly degenerate [81] at the frequency  $\sqrt{4 + \gamma_0}$  and located at three corners of the finite triangular lattice, as shown in Fig. 1(c). One unique characteristic of these corner states is that every alternate (even) site from the corner exhibits zero displacement [76]. Meanwhile, the profiles of the two edge states corresponding to the two highest eigenfrequencies in the edge spectrum are displayed in Fig. 1(d). Interestingly, these two edge states have nearly the

same eigenfrequencies. The first edge state exhibits maximum displacements localized at the left and right edges of the triangle, while the latter has them at the bottom edge. In the following sections, we will not only focus on how nonlinearity affects the corner states but also explore its impact on edge states, which may lead to the emergence of new classes of corner states in nonlinear lattices.

### III. NONLINEAR CONTINUATION

In this analysis, we apply a strong hardening nonlinearity with  $\alpha = 0.8$  to the grounded springs of the kagome lattice to investigate its influence on corner and edge states. We utilize a Newton solver to numerically obtain nonlinear periodic solutions at various frequencies, thereby revealing the nonlinear normal modes (NNMs). For clarity, we term NNMs obtained by the nonlinear continuation of the corner state as “NNM<sub>c</sub>” and the edge state as “NNM<sub>e</sub>” in subsequent sections. Additionally, we determine the linear stability of these NNMs using Floquet theory and analyze the nature of instabilities through the examination of Floquet multipliers (FMs). All numerical methods employed for the determination of NNMs and their stability are described in Appendix B.

#### A. Continuation of corner state

Since we had observed three nearly degenerate corner states in Fig. 1(c), we now prepare a new corner state localized at only one (top) corner of the lattice through linear superposition. This state is then provided as the initial condition to the Newton solver. We make this choice for simplicity as we investigate a family of high-amplitude corner states at only one corner region. It is important to note that this approach remains valid for a large lattice, where coupling effects between states localized at different corners are negligible. Figure 2(a) displays a frequency-energy plot illustrating the evolution of NNM<sub>c</sub> as the lattice energy in the system increases. The lattice energy represents the summation of the kinetic energy of all the masses and the total strain energy stored in intercell, intracell, and grounded springs (see Appendix C). We observe that the frequency of the NNM<sub>c</sub> increases with the total energy in the system due to the hardening nature of nonlinearity, as observed in a one-dimensional nonlinear chain [27,29]. Moreover, they enter the optical band at higher energy levels and resonate with bulk states, resulting in a decrease in slope as the total energy rises.

The linear stability of NNM<sub>c</sub> varies within the band gap, as depicted in Fig. 2(b), where the maximum amplitude of FMs is plotted as a function of frequency. It is well known that periodic solutions remain linearly stable when the maximum amplitude of FMs is less than or equal to unity, but instability arises when it exceeds unity. Initially, the NNM<sub>c</sub> remain stable up to  $\omega = 2.84$  due to weak nonlinear effects. In this range, the profile of the NNM<sub>c</sub> is similar to that of a corner state in the linear limit, as shown in Fig. 2(c). However, beyond  $\omega = 2.84$ , the NNM<sub>c</sub> become unstable until about  $\omega = 2.89$ , as depicted in Fig. 2(b). In this region, FMs deviate slightly from unity, implying very weak instability. These are *finite-size instabilities* [84], which are expected to reduce further as the size of the system increases (see Appendix D for more

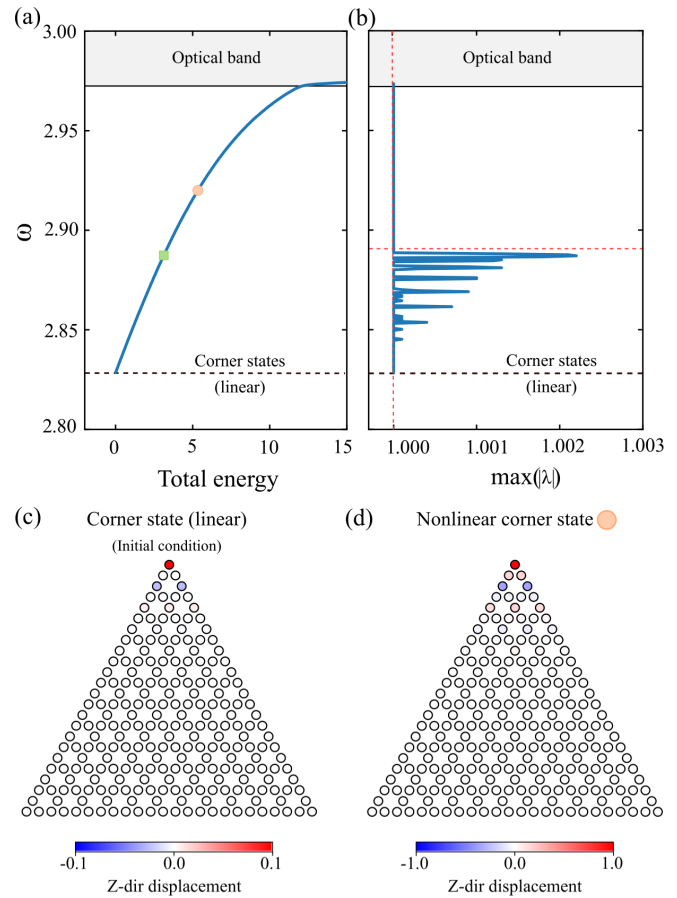


FIG. 2. Nonlinear continuation of the corner state. (a) Frequency-energy plot showing the evolution of NNM<sub>c</sub> with lattice energy. (b) Maximum absolute value of Floquet multipliers “ $\lambda$ ” describing the stability of periodic solutions, becoming unstable when they exceed unity (vertical dashed line). The red horizontal dashed line indicates the beginning of the stable region. (c) The initial condition for numerical continuation obtained by the superposition of three corner states in the linear limit. (d) Profile of the NNM<sub>c</sub> measured at  $\omega = 2.92$ , as indicated by the circular marker in (a). It shows a high-amplitude corner state. The color bar denotes the out-of-plane displacements of the masses on an actual scale.

details). The profile in this range appears to be localized around the corner of the lattice; hence the NNM<sub>c</sub> can also be referred to as a nonlinear corner state. Interestingly, for  $\omega > 2.89$ , NNM<sub>c</sub> becomes stable inside the band gap with a high amplitude of vibration. Figure 2(d) shows one such stable high-amplitude corner state at  $\omega = 2.92$ . Importantly, these high-amplitude corner states exhibit nonzero displacements at even sites from the top corner—a feature that distinguishes them from corner states in the linear limit.

To demonstrate the linear stability of NNM<sub>c</sub>, we conduct long-time transient simulations for a duration of  $2 \times 10^5 T$ , where  $T$  represents the time period of NNM<sub>c</sub>. At first, the NNM<sub>c</sub> at  $\omega = 2.887$  is used as the initial condition, with the addition of white noise at an amplitude of 1% of the displacement. Figure 3(a) presents the short-time Fourier transform (STFT) obtained from the time history of the top particle,

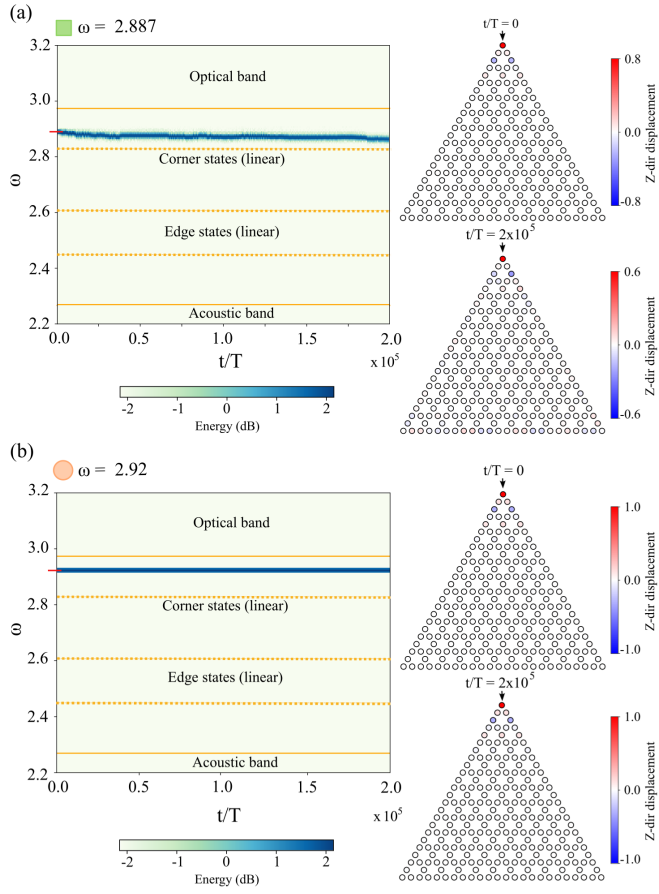


FIG. 3. Transient analysis of  $\text{NNM}_c$  to demonstrate its stability nature. (a) Short-time Fourier transform (STFT) of the displacement measured at the top particle (marked with a black arrow) for a frequency of  $\omega = 2.887$ . The instability in this state results in a gradual downshift of frequency towards a new state over time. (b) STFT of the displacement measured at the same particle for a frequency of  $\omega = 2.92$ , maintaining the same state over an extended period, indicating its stable nature. The color bar represents the total energy in the system, expressed in decibels (dB). Profiles at the initial time ( $t = 0$ ) and the final time ( $t = 2 \times 10^5 T$ ) are also included for both (a) and (b).

marked with a black arrow. Since this  $\text{NNM}_c$  is linearly unstable, it deviates from the initial frequency and slowly moves towards a low-frequency state that is stable. The spatial profile at  $t/T = 2 \times 10^5$  is also depicted in Fig. 3(a), resembling the  $\text{NNM}_c$  at  $\omega = 2.863$ , which falls inside the small stable region within the frequency range of 2.84–2.89. Now we present the STFT of the same particle when the  $\text{NNM}_c$  at  $\omega = 2.92$  is given as the initial condition. Since this state is linearly stable, from Fig. 3(b), it is evident that the frequency of the state remains constant and maintains the initial state over an extended period. Therefore, we have verified the existence of stable high-amplitude corner states within the band gap.

### B. Continuation of edge state

We use an edge state, depicted in the first part of Fig. 1(d), as the initial condition for the Newton solver. The frequency-energy plot and the stability diagram of the  $\text{NNM}_e$  are

illustrated in Figs. 4(a) and 4(b). Interestingly, as the total energy increases, the edge state transforms into various types of states localized at the corner of the lattice. This transformation is evident from their profiles, as depicted in Fig. 4(c). Hence, for this particular edge state, the  $\text{NNM}_e$  can also be referred to as a nonlinear corner state. At lower, intermediate, and higher frequencies, we observe one, three, and five types of nonlinear corner states, respectively. The differences in these nonlinear corner states can be explained using the asymmetry coefficient,  $\Theta$ , defined as [85]

$$\Theta = \frac{E_{g1} - E_{g2}}{E_{g1} + E_{g2}}, \quad (2)$$

where  $E_{g1}$  and  $E_{g2}$  represent the potential energies stored in the grounded springs when undergoing deformations in positive and negative  $Z$  directions, respectively. It satisfies the relation  $E_g = E_{g1} + E_{g2}$ , where  $E_g$  is the total potential energy stored in the grounded springs (see Appendix C). Therefore, for a particular nonlinear corner state,  $\Theta$  examines the symmetry in energy distribution about the X-Y plane. As depicted in Figs. 4(a) and 4(b), the frequency of the  $\text{NNM}_e$  increases and they undergo different bifurcations as the lattice energy is increased. The  $\text{NNM}_e$  remains stable until  $\omega = 2.637$  (marked by the thick purple line), although minor finite-size instabilities persist within this range. The profile just below a frequency of  $\omega = 2.637$  is shown in Fig. 4(c), indicated by a square marker. It reveals an entirely new class of corner states, distinct from the  $\text{NNM}_c$  discussed in the previous section. A zero displacement occurs at the corner mass and the displacements on the left edge are in antiphase with those on the right edge. This illustrates the symmetric nature ( $\Theta = 0$ ) of the state about the X-Y plane.

Increasing the energy further, a bifurcation occurs at  $\omega = 2.637$ , leading to the separation of the stable symmetric branch into an unstable symmetric branch (indicated by the dashed purple line) and two stable asymmetric branches (represented by the thick green line). As the energies of both asymmetric branches are equal, they overlap in the energy plot. This bifurcation point is a symmetry-breaking point, denoted as “SB<sub>1</sub>” in subsequent diagrams. Figures 4(d) and 4(e) illustrate zoomed sections of the energy plot and the asymmetry coefficient plotted around the point SB<sub>1</sub>. In Fig. 4(e), two distinct curves are presented for the stable asymmetric branches since the signs of  $\Theta$  are opposite to each other. They clearly show a pitchfork bifurcation occurring at SB<sub>1</sub>, resulting in two stable states and one unstable state beyond SB<sub>1</sub>. Upon tracing these stable branches, we observe that the magnitude of the asymmetry coefficient increases with frequency and exhibits strong asymmetry at large  $\omega$ . This is evident from their profiles, highlighted with triangular markers in Fig. 4(c). We now observe a nonzero displacement at the top corner mass and the displacements at the left and right edges differ in magnitude and phase. Hence this represents a new type of nonlinear corner state. With the increase in energy, finite instabilities become more significant until a frequency of  $\omega = 2.816$ . However, the magnitude of such instabilities is small compared to other types of instabilities. Therefore, these high-amplitude corner states can remain stable within this frequency range when a large triangular lattice is constructed.

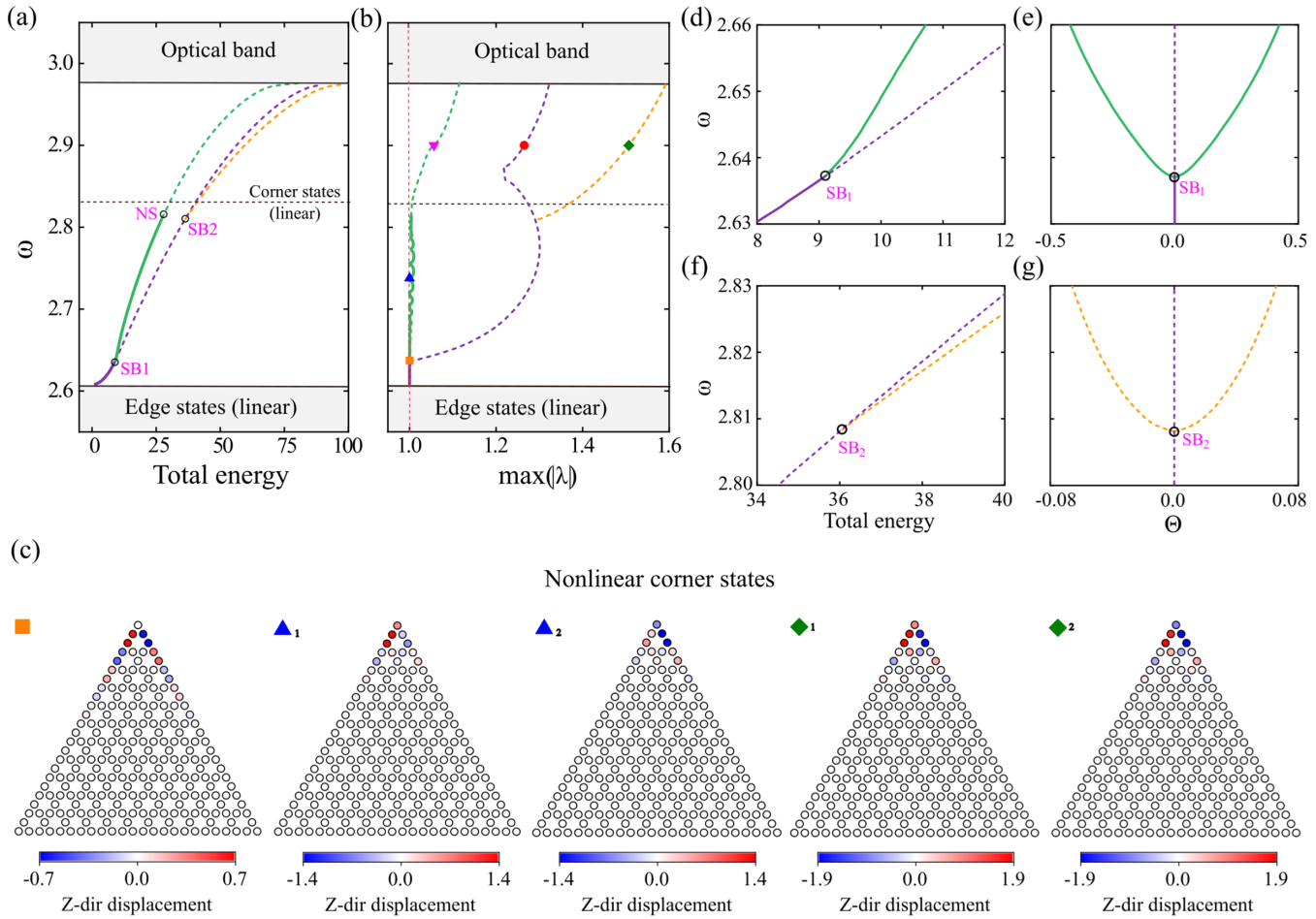


FIG. 4. Nonlinear continuation of the edge state. (a) Frequency-energy plot showing the evolution of  $NNM_e$  with lattice energy. It splits into different branches as the energy in the system increases, depicted using different colors. The bifurcation points on these branches are labeled as  $SB_1$ ,  $SB_2$ , and  $NS$ . (b) Maximum absolute value of Floquet multipliers “ $\lambda$ ” as a function of  $\omega$ , describing the stability of periodic solutions. The stable solutions are shown by thick lines, while unstable solutions are indicated by dashed lines. (c) The profiles of various  $NNM_e$ , measured at the frequencies indicated by different markers in (b), show distinct states localized at the corner of the lattice. The color bar denotes the out-of-plane displacements of the masses on an actual scale. (d)–(g) Zoomed sections of the energy plot and asymmetry coefficient “ $\Theta$ ” varied with frequency around  $SB_1$  and  $SB_2$ , respectively.

Beyond  $\omega = 2.816$ , a qualitative change in the  $NNM_e$  occurs, wherein the magnitude of instability starts to increase rapidly (represented by a dashed green line). While analyzing the FMs, we observe that a pair of Floquet multipliers begins to leave the unit circle along the complex plane as the energy is increased (see Appendix D for more details). This is an *oscillatory instability* and occurs due to Neimark-Sacker bifurcation at  $\omega = 2.816$ , denoted by “ $NS$ ” in the plot. Therefore, the  $NNM_e$  appearing beyond  $NS$  are largely unstable. Furthermore, this unstable branch enters the optical band at high-energy levels and resonates with the bulk states.

Following the unstable symmetric branch beyond  $SB_1$ , we find that the FMs leave the unit circle along the real axis. This represents a *real instability*, which increases rapidly with increasing energy. Throughout this branch, the nonlinear corner states maintain their symmetry. With further increase in energy, a second symmetry-breaking event ( $SB_2$ ) occurs at  $\omega = 2.808$ . The unstable symmetric branch then splits into two unstable asymmetric branches (represented by the dashed orange line) and an unstable symmetric branch (indicated

by the dashed purple line). Similar to the previous bifurcation, the asymmetric branches overlap in the energy plot and present two distinct curves in the asymmetry plot, as shown in Figs. 4(f) and 4(g). It exhibits a pitchfork-like structure but with all unstable branches. The profiles on these unstable asymmetric branches are plotted in Fig. 4(c), with diamond markers. Compared to the symmetric nonlinear corner state, these new states exhibit a nonzero displacement at the top corner mass, while the remaining masses have the same displacements. Hence the value of the asymmetry coefficient is very small, as seen in Fig. 4(g). Moreover, these asymmetric corner states are in antiphase with each other at the top corner mass, vibrating in opposite directions at the same frequency.

To explore the evolution of these  $NNM_e$  over time, a long-time transient simulation is carried out for  $t = 0.5 \times 10^5 T$ . The STFT obtained from the time history of a specific particle (marked with a black arrow) is provided in Figs. 5(a)–5(d). For the stable  $NNM_e$ , highlighted with a triangle marker in Fig. 4(c), the frequency of the state remains constant and

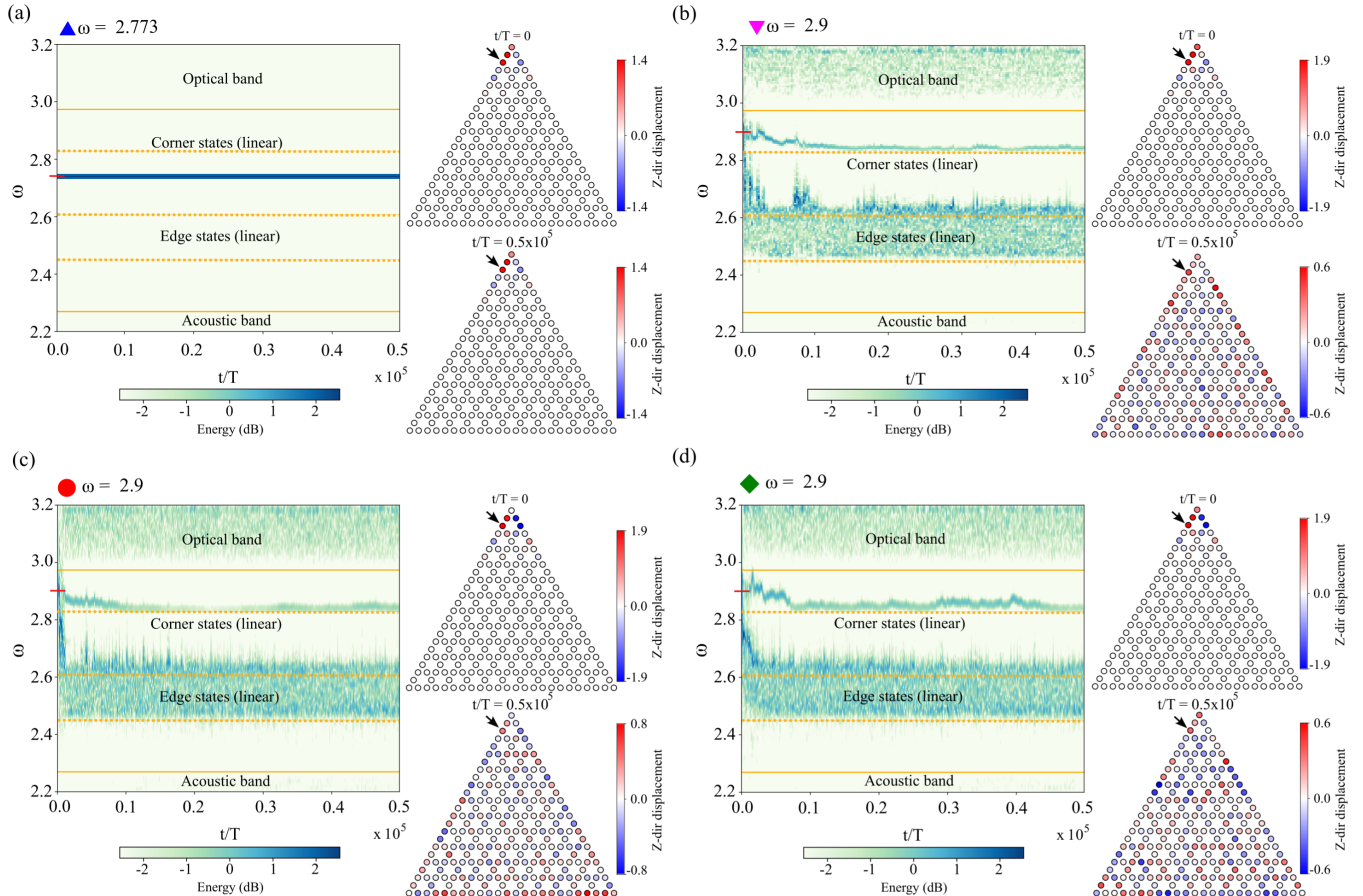


FIG. 5. Transient analysis of  $NNM_e$  to demonstrate its stability nature. (a) Short-time Fourier transform of the displacement measured at a specific particle (marked with a black arrow) on the stable  $NNM_e$ , indicated using a triangle marker in Fig. 4. The frequency remains constant and the  $NNM_e$  maintains its shape throughout the period. (b)–(d) STFT of the displacement measured at the same particle, but for unstable  $NNM_e$  highlighted in Fig. 4. It deviates from the initial state quickly since the magnitude of instability is high. The final state contains the frequencies of linear corner states, edge states, and bulk states. The color bar represents the total energy in the system, expressed in decibels (dB). Profiles at the initial time ( $t = 0$ ) and the final time ( $t = 0.5 \times 10^5 T$ ) are also included.

maintains its shape over time. However, for unstable  $NNM_e$ , the frequency quickly deviates from that of the initial state due to the high magnitude of instability. Moreover, the final state contains frequencies corresponding to linear corner states, edge states, and bulk states, resulting in a complex profile. Thus, among the five types of corner states obtained through the continuation of the edge state, only two types of nonlinear corner states (marked with triangles) remain stable at high frequencies.

#### IV. CONCLUSIONS

In this paper, we investigate a HOTI composed of kagome lattice that supports edge and corner states in the linear limit. We examine the existence and stability of high-amplitude corner states resulting from cubic on-site nonlinearity. We perform nonlinear continuation for both the corner state and the edge state to obtain their NNMs. Our findings indicate that the NNMs from the continuation of the corner state can be linearly stable in a specific frequency regime, hinting at robust, high-amplitude energy localization at the corners.

Additionally, we observe different families of high-amplitude corner states when an edge state is continued into the nonlinear regime. This phenomenon occurs through two pitchfork bifurcations, transforming a symmetric corner state into two asymmetric corner states and one symmetric corner state. Some of them remain stable, while others lose their stability through real instability and Neimark-Sacker bifurcation.

The key finding of this work is the possibility of different classes of high-amplitude corner states bifurcating from the edge state under nonlinear conditions. This phenomenon depends on the type of nonlinearity in the lattice. Therefore, investigating the role of intersite nonlinearity and different forms of nonlinearity on the bifurcation and stability of high-amplitude corner states will be an interesting avenue for future research. For the experimental observation of such stable high-amplitude corner states, future work could focus on designing a setup with minimal losses and exciting the corner with large-amplitude initial conditions. Additionally, for highly damped lattices, a driven-damped setting [23] could also be explored to excite nonlinear corner states. Finally, such topological lattices can also be useful for a systematic

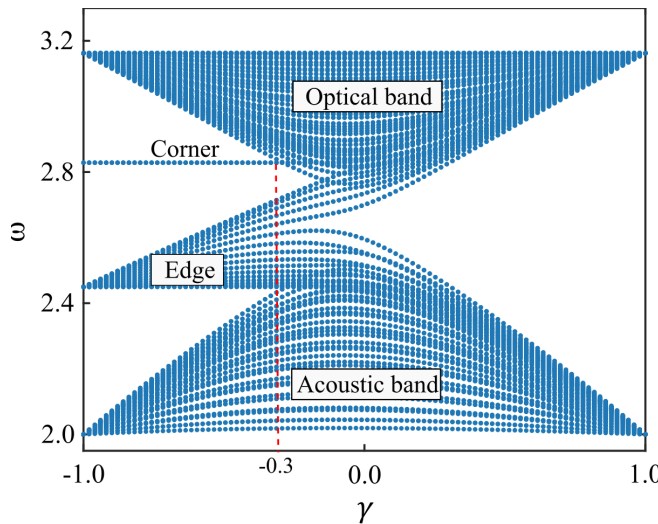


FIG. 6. Eigenspectrum for a triangular-shaped kagome lattice plotted as a function of stiffness differential  $\gamma$ .

exploration of the interplay between nonlinearity and non-Hermiticity [86,87] on the corner states.

#### ACKNOWLEDGMENTS

R.C. acknowledges funding support by the Science and Engineering Research Board (SERB), India, through the Start-up Research Grant No. SRG/2022/001662. K.P. acknowledges support from the Institute of Eminence (IoE) IISc Postdoctoral Fellowship.

#### APPENDIX A: EIGENSPECTRUM OF THE FINITE KAGOME LATTICE AS A FUNCTION OF STIFFNESS DIFFERENTIAL

The eigenspectrum of a finite kagome lattice of triangular shape is shown in Fig. 6 for different values of  $\gamma$ , ranging from  $-1$  to  $1$ . Since the system is a *nontrivial HOTI* for  $\gamma < -0.3$ , we observe the emergence of corner states inside the band gap.

#### APPENDIX B: NUMERICAL METHODS

In this Appendix, we present the numerical methods used to determine the NNM and assess the stability of our model. The governing equation for a nonlinear system with  $N$  degrees of freedom can be written in state-space form as follows:

$$\dot{\mathbf{q}} = F(\mathbf{q}), \quad (\text{B1})$$

where  $\mathbf{q}$  is the state vector that contains the displacement and velocity of the masses in the lattice.

*Continuation method.* We use the parameter continuation technique [23,27,88–90] to obtain NNMs at different frequen-

cies,  $\omega$ . Starting with a known solution (near a linear state), we increment the parameter  $\omega$  by a small step  $\Delta\omega$  to obtain the response after one time period  $T = 2\pi/\omega$ . Using the Newton-Raphson method, we obtain a periodic solution iteratively by satisfying

$$\Phi[\mathbf{q}(0)] = \mathbf{q}(0) - \mathbf{q}(T) = \mathbf{0}, \quad (\text{B2})$$

where the residual,  $\Phi$ , is a function of initial condition  $\mathbf{q}(0)$ . The Jacobian for the solver can be obtained by differentiating Eq. (B2) with respect to  $\mathbf{q}(0)$  as follows:

$$\frac{\partial \Phi}{\partial \mathbf{q}(0)} = \mathbf{I} - \frac{\partial \mathbf{q}(t)}{\partial \mathbf{q}(0)}_{t=T} = \mathbf{I} - \mathbf{V}(T), \quad (\text{B3})$$

where  $\mathbf{I}$  is the identity matrix and  $\mathbf{V}(T)$  can be obtained by integrating the variational equation,

$$\frac{d\mathbf{V}}{dt} = \mathbf{J}(t)\mathbf{V} \quad (\text{B4})$$

simultaneously with Eq. (B1). Here,  $\mathbf{J}$  is the Jacobian of the governing nonlinear equations and  $\mathbf{V}(0) = \mathbf{I}$ .

*Stability analysis.* The linear stability of these NNMs is assessed by monitoring the evolution of a small perturbation  $d\mathbf{q}$ , around the periodic solution  $\mathbf{q}_0$ . Thus, by substituting  $\mathbf{q} = \mathbf{q}_0 + d\mathbf{q}$ , we derive the system of variational equations

$$d\mathbf{q} = \left( \frac{\partial F}{\partial \mathbf{q}} \right)_{\mathbf{q}=\mathbf{q}_0} d\mathbf{q}. \quad (\text{B5})$$

The perturbation after  $m$  time periods can be obtained as

$$d\mathbf{q}(mT) = [\mathbf{V}(T)]^m d\mathbf{q}(0), \quad (\text{B6})$$

where  $\mathbf{V}(T)$  is the *monodromy matrix*, which is already obtained during the Newton-Raphson solution process, as given in Eq. (B4). The eigenvalues of the monodromy matrix are called Floquet multipliers (FMs)  $\lambda$ .  $|\lambda| > 1$  indicates growing perturbations, i.e., instability.

*Branch switching.* At the bifurcation point, there exist one or more Floquet multipliers with a modulus greater than one, indicating instability. We use the corresponding Floquet eigenvector as a small perturbation to the original periodic solution and obtain the new branch. The continuation method is then followed on the new branch.

#### APPENDIX C: CALCULATION OF LATTICE ENERGY

As mentioned in the main text, the lattice energy represents the summation of the kinetic energy of all the masses ( $E_m$ ) and the total strain energy stored in intercell ( $E_{\text{inter}}$ ), intracell ( $E_{\text{intra}}$ ), and grounded springs ( $E_g$ ). Therefore, the total energy  $E_{\text{tot}}$  of a finite kagome lattice having  $N_{\text{tot}}$  unit cells can be expressed as

$$E_{\text{tot}} = \sum_{N_{\text{tot}}} [E_m + E_{\text{intra}} + E_{\text{inter}} + E_g], \quad (\text{C1})$$

where

$$E_m = \frac{1}{2} (\dot{u}_{1_{m,n}}^2 + \dot{u}_{2_{m,n}}^2 + \dot{u}_{3_{m,n}}^2),$$

$$E_{\text{intra}} = \frac{1}{2} (1 + \gamma) \left[ (u_{1_{m,n}} - u_{2_{m,n}})^2 + (u_{2_{m,n}} - u_{3_{m,n}})^2 + (u_{3_{m,n}} - u_{1_{m,n}})^2 \right],$$

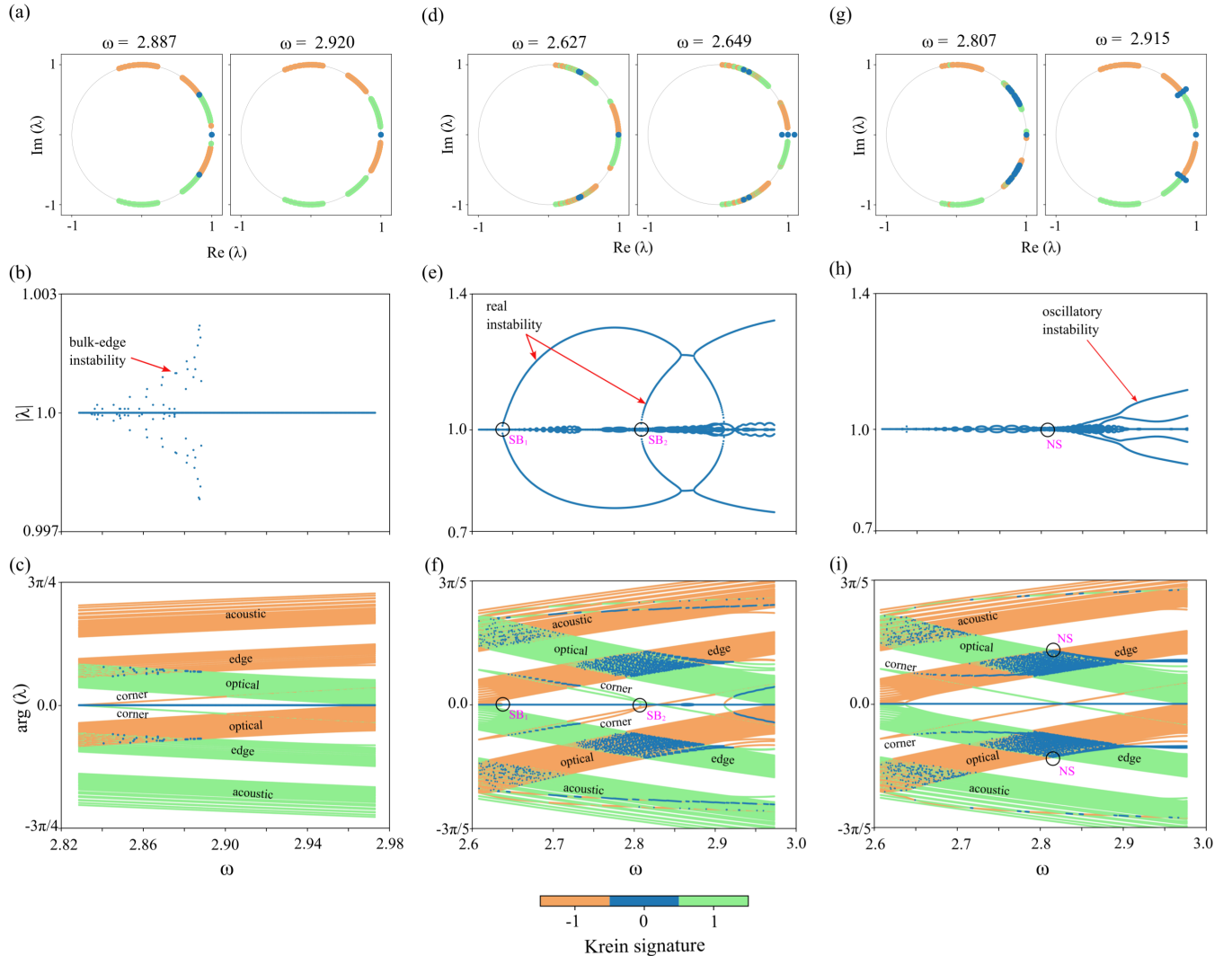


FIG. 7. Variation in FMs with an increase in frequency. (a) FMs at two specified frequencies are presented in the complex plane for NNMs obtained through the continuation of corner state. The color indicates the Krein signature of each FM. (b) Variations in the absolute value of FMs as the frequency increases. When  $|\lambda|$  exceeds unity, the system becomes unstable. Types of instabilities are also indicated. (c) Variations in the phase of FMs with frequency. Blue dots represent FMs with zero Krein signature, indicating instability. (d)–(i) Similar plots are provided for the two branches of NNMs obtained through the continuation of edge state. The circle marker shows the bifurcation points.

$$E_{\text{inter}} = \frac{1}{2}(1 - \gamma)[\epsilon_1(u_{1,m,n} - u_{2,m+1,n})^2 + \epsilon_2(u_{1,m,n} - u_{3,m,n-1})^2 + \epsilon_3(u_{2,m,n} - u_{3,m-1,n})^2 + \epsilon_4(u_{2,m,n} - u_{1,m-1,n+1})^2 + \epsilon_5(u_{3,m,n} - u_{1,m,n+1})^2 + \epsilon_6(u_{3,m,n} - u_{2,m+1,n})^2],$$

$$E_g = \frac{1}{2}\gamma_0(u_{1,m,n}^2 + u_{2,m,n}^2 + u_{3,m,n}^2) + \frac{1}{4}\alpha(u_{1,m,n}^4 + u_{2,m,n}^4 + u_{3,m,n}^4).$$

Here,  $\epsilon_i$  accounts for the boundary condition:  $\epsilon_i = 1$  if the spring is fixed at the boundaries and  $\epsilon_i = 0.5$  otherwise.

#### APPENDIX D: TYPE OF INSTABILITIES IN THE SYSTEM

Typically, the instabilities in the system are determined by analyzing the FMs of the NNMs. When we plot the FMs in the complex plane, they lie on or inside the unit circle for a stable system. Instability arises when some FMs start to leave the unit circle. This can occur in two ways: when two complex conjugate FMs collide on the real axis and leave the

unit circle along the real axis or when two pairs of complex conjugate FMs collide elsewhere on the unit circle and leave the unit circle as a quadruplet of FMs. The first type of instability is called *real instability* and the latter one is called *oscillatory instability*. Moreover, each FM has its associated Krein signature, which can be defined as the sign of the Krein product of the corresponding eigenvector  $v$ . It is calculated as follows [91]:

$$K(\lambda) = \text{sgn}[v^\dagger(-iJ)v], \quad (\text{D1})$$

where  $i$  and  $\dagger$  represent the imaginary unity and the complex transpose, respectively. The symplectic matrix  $J = \begin{bmatrix} 0 & I_N \\ -I_N & 0 \end{bmatrix}$ , with  $I_N$  being the identity matrix of dimension  $N$ . Krein signature can be either +1 or -1 for FMs lying on the unit circle, except for the one at  $(+1, 0)$  where it is zero. A necessary condition for instability to arise is that FMs with opposing Krein signatures must collide and depart from the unit circle [92,93]. Consequently, FMs leaving the circle also have a zero Krein signature, indicating instability.

Now, we examine the types of instabilities that arise in our system. Figure 7(a) shows the FMs of  $NNM_c$ , measured at  $\omega = 2.887$  and  $2.92$ . In Fig. 7(a), we observe that, at  $\omega = 2.887$ , FMs with opposite Krein signatures (orange and green arcs) collide with each other and leave the unit circle with a zero Krein signature (blue). Since the collision occurs at a point other than the real axis, it represents an *oscillatory instability*. Due to the very small magnitude of this instability, these FMs appear to lie on the unit circle. However, at  $\omega = 2.92$ , the FMs do not collide with each other and there are no FMs with zero Krein signature outside the unit circle, indicating that the state is linearly stable.

To verify this further, we plot the variations in FMs as a function of frequency. Figures 7(b) and 7(c) depict how the absolute value ( $|\lambda|$ ) and argument [ $\arg(\lambda)$ ] of FMs change with increasing frequency. Within the frequency range of 2.84–2.89,  $|\lambda|$  exceeds unity and there exists a collision between spectral bands of opposite Krein signatures (orange and green). This collision induces instabilities in the system, characterized by a zero Krein signature (blue). We can identify states associated with each spectral band since they are related to the eigenspectrum of the linear system, as reported in Ref. [27]. In Fig. 7(c), these states are marked on each spectral band. Since the collision occurs between the bulk and edge states, we term this instability the “bulk-edge instability.” Such instabilities decrease in strength as the size of the system increases and are expected to vanish in the infinite lattice limit [84]. Hence they are also called *finite-size instabilities*. Beyond  $\omega = 2.89$ , no collisions of states (no blue dots) are observed, although the corner states intersect bulk states in

this frequency range. Therefore, these states are stable, as presented in the main text.

We conduct a similar investigation for the  $NNM_e$ . In Fig. 7(d), the FMs of symmetric nonlinear corner states [represented by the purple line in Fig. 4(a)] are plotted in the complex plane for  $\omega = 2.627$  and  $2.649$ . Notably, at  $\omega = 2.627$ , some FMs with a zero Krein signature lie close to the unit circle, indicating *finite-size instability*. In contrast, at  $\omega = 2.649$ , an FM with a zero Krein signature lies outside the unit circle on the real axis, suggesting *real instability*. Furthermore, we plot  $|\lambda|$  and  $\arg(\lambda)$  as functions of frequency in Figs. 7(e) and 7(f). Within the frequency range of 2.607–2.637, collisions between two bulk states from acoustic and optical bands occur, resulting in finite-size instabilities of very small magnitude. At  $\omega = 2.637$ , we observe two complex conjugate FMs colliding on the real axis. This collision point is  $SB_1$ . It is a bifurcation point beyond which the FMs depart from the unit circle along the real axis. Subsequently, the magnitude of instability increases rapidly, confirming real instability. Moreover, a second bifurcation occurs at  $\omega = 2.808$ , where two complex conjugate FMs collide again on the real axis. This point is represented by  $SB_2$ . In short, real instabilities dominate in the system beyond  $\omega = 2.637$ , although some finite-size instabilities also persist.

Figures 7(g)–7(i) depict the FMs of asymmetric corner states [indicated by the green line in Fig. 4(a)] plotted against frequency. Finite-size instabilities are observed within the system up to a frequency of  $\omega = 2.816$ , after which oscillatory instabilities emerge. This is evident in Fig. 7(g), where FMs with zero Krein signature are notably positioned outside the unit circle, particularly at  $\omega = 2.915$ . In Figs. 7(h) and 7(i), it becomes apparent that the onset of oscillatory instability occurs when an isolated FM emerges from a spectral band (marked with a circle). This marked point, representing the onset of oscillatory instability, is identified as a bifurcation point known as the Neimark-Sacker bifurcation (NS). The magnitude of such instability increases with the increase in frequency.

- 
- [1] W. A. Benalcazar, B. A. Bernevig, and T. L. Hughes, Quantized electric multipole insulators, *Science* **357**, 61 (2017).
  - [2] W. A. Benalcazar, B. A. Bernevig, and T. L. Hughes, Electric multipole moments, topological multipole moment pumping, and chiral hinge states in crystalline insulators, *Phys. Rev. B* **96**, 245115 (2017).
  - [3] F. Schindler, A. M. Cook, M. G. Vergniory, Z. Wang, S. S. Parkin, B. A. Bernevig, and T. Neupert, Higher-order topological insulators, *Sci. Adv.* **4**, eaat0346 (2018).
  - [4] C. W. Peterson, W. A. Benalcazar, T. L. Hughes, and G. Bahl, A quantized microwave quadrupole insulator with topologically protected corner states, *Nature (London)* **555**, 346 (2018).
  - [5] M. Serra-Garcia, V. Peri, R. Süsstrunk, O. R. Bilal, T. Larsen, L. G. Villanueva, and S. D. Huber, Observation of a phononic quadrupole topological insulator, *Nature (London)* **555**, 342 (2018).
  - [6] W. A. Benalcazar, T. Li, and T. L. Hughes, Quantization of fractional corner charge in  $C_n$ -symmetric higher-order topological crystalline insulators, *Phys. Rev. B* **99**, 245151 (2019).
  - [7] J. A. Medina-Vázquez, Influence of asymmetric long-range interactions on corner states in photonic higher-order topological insulators, *Phys. Rev. A* **107**, 043503 (2023).
  - [8] J. A. Medina-Vázquez, E. Y. González-Ramírez, and J. G. Murillo-Ramírez, Corner states in photonic higher-order Dirac semimetals, *Phys. Rev. A* **107**, 053511 (2023).
  - [9] M. Proctor, M. B. de Paz, D. Bercioux, A. García-Etxarri, and P. A. Huidobro, Higher-order topology in plasmonic Kagome lattices, *Appl. Phys. Lett.* **118**, 091105 (2021).
  - [10] Z. Ma, Y. Liu, Y.-X. Xie, and Y.-S. Wang, Tuning of higher-order topological corner states in a honeycomb elastic plate, *Phys. Rev. Appl.* **19**, 054038 (2023).

- [11] L. Zhou and W. Yu, Visualization of rainbow trapping effect in higher-order topological insulators, *Phys. Rev. B* **107**, 174105 (2023).
- [12] J.-X. Yin, B. Lian, and M. Z. Hasan, Topological Kagome magnets and superconductors, *Nature (London)* **612**, 647 (2022).
- [13] E. Tang, J. Agudo-Canalejo, and R. Golestanian, Topology protects chiral edge currents in stochastic systems, *Phys. Rev. X* **11**, 031015 (2021).
- [14] M. Ezawa, Non-Hermitian higher-order topological states in nonreciprocal and reciprocal systems with their electric-circuit realization, *Phys. Rev. B* **99**, 201411(R) (2019).
- [15] H. Yang, Z.-X. Li, Y. Liu, Y. Cao, and P. Yan, Observation of symmetry-protected zero modes in topoelectrical circuits, *Phys. Rev. Res.* **2**, 022028(R) (2020).
- [16] B. Xie, H.-X. Wang, X. Zhang, P. Zhan, J.-H. Jiang, M. Lu, and Y. Chen, Higher-order band topology, *Nat. Rev. Phys.* **3**, 520 (2021).
- [17] D. Smirnova, D. Leykam, Y. Chong, and Y. Kivshar, Nonlinear topological photonics, *Appl. Phys. Rev.* **7**, 021306 (2020).
- [18] M. J. Ablowitz, C. W. Curtis, and Y.-P. Ma, Linear and nonlinear traveling edge waves in optical honeycomb lattices, *Phys. Rev. A* **90**, 023813 (2014).
- [19] D. Leykam and Y. D. Chong, Edge solitons in nonlinear photonic topological insulators, *Phys. Rev. Lett.* **117**, 143901 (2016).
- [20] Y. V. Kartashov and D. V. Skryabin, Modulational instability and solitary waves in polariton topological insulators, *Optica* **3**, 1228 (2016).
- [21] D. A. Dobrykh, A. V. Yulin, A. P. Slobozhanyuk, A. N. Poddubny, and Y. S. Kivshar, Nonlinear control of electromagnetic topological edge states, *Phys. Rev. Lett.* **121**, 163901 (2018).
- [22] R. K. Pal, J. Vila, M. Leamy, and M. Ruzzene, Amplitude-dependent topological edge states in nonlinear phononic lattices, *Phys. Rev. E* **97**, 032209 (2018).
- [23] J. Vila, G. H. Paulino, and M. Ruzzene, Role of nonlinearities in topological protection: Testing magnetically coupled fidget spinners, *Phys. Rev. B* **99**, 125116 (2019).
- [24] D. D. Snee and Y.-P. Ma, Edge solitons in a nonlinear mechanical topological insulator, *Extreme Mech. Lett.* **30**, 100487 (2019).
- [25] A. Darabi and M. J. Leamy, Tunable nonlinear topological insulator for acoustic waves, *Phys. Rev. Appl.* **12**, 044030 (2019).
- [26] S. Mukherjee and M. C. Rechtsman, Observation of unidirectional solitonlike edge states in nonlinear floquet topological insulators, *Phys. Rev. X* **11**, 041057 (2021).
- [27] R. Chaunsali, H. Xu, J. Yang, P. G. Kevrekidis, and G. Theocharis, Stability of topological edge states under strong nonlinear effects, *Phys. Rev. B* **103**, 024106 (2021).
- [28] Y.-P. Ma and H. Susanto, Topological edge solitons and their stability in a nonlinear Su-Schrieffer-Heeger model, *Phys. Rev. E* **104**, 054206 (2021).
- [29] J. R. Tempelman, K. H. Matlack, and A. F. Vakakis, Topological protection in a strongly nonlinear interface lattice, *Phys. Rev. B* **104**, 174306 (2021).
- [30] Y. V. Kartashov, A. A. Arkhipova, S. A. Zhuravitskii, N. N. Skryabin, I. V. Dyakonov, A. A. Kalinkin, S. P. Kulik, V. O. Kompanets, S. V. Chekalin, L. Torner, and V. N. Zadkov, Observation of edge solitons in topological trimer arrays, *Phys. Rev. Lett.* **128**, 093901 (2022).
- [31] C. Li and Y. V. Kartashov, Topological gap solitons in Rabi Su-Schrieffer-Heeger lattices, *Phys. Rev. B* **108**, 184301 (2023).
- [32] B. Michen and J. C. Budich, Nonlinear interference challenging topological protection of chiral edge states, *Phys. Rev. A* **108**, L021501 (2023).
- [33] M. I. Rosa, M. J. Leamy, and M. Ruzzene, Amplitude-dependent edge states and discrete breathers in nonlinear modulated phononic lattices, *New J. Phys.* **25**, 103053 (2023).
- [34] S. Kruk, A. Poddubny, D. Smirnova, L. Wang, A. Slobozhanyuk, A. Shorokhov, I. Kravchenko, B. Luther-Davies, and Y. Kivshar, Nonlinear light generation in topological nanostructures, *Nat. Nanotechnol.* **14**, 126 (2019).
- [35] Y. Wang, L.-J. Lang, C. H. Lee, B. Zhang, and Y. Chong, Topologically enhanced harmonic generation in a nonlinear transmission line metamaterial, *Nat. Commun.* **10**, 1102 (2019).
- [36] D. Zhou, J. Ma, K. Sun, S. Gonella, and X. Mao, Switchable phonon diodes using nonlinear topological maxwell lattices, *Phys. Rev. B* **101**, 104106 (2020).
- [37] Y. Lumer, Y. Plotnik, M. C. Rechtsman, and M. Segev, Self-localized states in photonic topological insulators, *Phys. Rev. Lett.* **111**, 243905 (2013).
- [38] D. D. Solnyshkov, O. Bleu, B. Teklu, and G. Malpuech, Chirality of topological gap solitons in bosonic dimer chains, *Phys. Rev. Lett.* **118**, 023901 (2017).
- [39] J. L. Marzuola, M. Rechtsman, B. Osting, and M. Bandres, Bulk soliton dynamics in bosonic topological insulators, *arXiv:1904.10312*.
- [40] S. Mukherjee and M. C. Rechtsman, Observation of Floquet solitons in a topological bandgap, *Science* **368**, 856 (2020).
- [41] D. A. Smirnova, L. A. Smirnov, D. Leykam, and Y. S. Kivshar, Topological edge states and gap solitons in the nonlinear Dirac model, *Laser Photon. Rev.* **13**, 1900223 (2019).
- [42] R. Chaunsali, P. G. Kevrekidis, D. Frantzeskakis, and G. Theocharis, Dirac solitons and topological edge states in the  $\beta$ -Fermi-Pasta-Ulam-Tsingou Dimer Lattice, *Phys. Rev. E* **108**, 054224 (2023).
- [43] L. Jezequel and P. Delplace, Nonlinear edge modes from topological one-dimensional lattices, *Phys. Rev. B* **105**, 035410 (2022).
- [44] S. Wong, T. A. Loring, and A. Cerjan, Probing topology in nonlinear topological materials using numerical k-theory, *Phys. Rev. B* **108**, 195142 (2023).
- [45] K. Bai, J.-Z. Li, T.-R. Liu, L. Fang, D. Wan, and M. Xiao, Arbitrarily configurable nonlinear topological modes, *Phys. Rev. Lett.* **133**, 116602 (2024).
- [46] Y. Hadad, A. B. Khanikaev, and A. Alu, Self-induced topological transitions and edge states supported by nonlinear staggered potentials, *Phys. Rev. B* **93**, 155112 (2016).
- [47] R. S. Savelev, M. A. Gorlach, and A. N. Poddubny, Topological interface states mediated by spontaneous symmetry breaking, *Phys. Rev. B* **98**, 045415 (2018).
- [48] R. Chaunsali and G. Theocharis, Self-induced topological transition in phononic crystals by nonlinearity management, *Phys. Rev. B* **100**, 014302 (2019).
- [49] G. D'Aguanno, Y. Hadad, D. A. Smirnova, X. Ni, A. B. Khanikaev, and A. Alù, Nonlinear topological transitions over a metasurface, *Phys. Rev. B* **100**, 214310 (2019).
- [50] L. J. Maczewsky, M. Heinrich, M. Kremer, S. K. Ivanov, M. Ehrhardt, F. Martinez, Y. V. Kartashov, V. V. Konotop, L.

- Torner, D. Bauer *et al.*, Nonlinearity-induced photonic topological insulator, *Science* **370**, 701 (2020).
- [51] G. Liu, J. Noh, J. Zhao, and G. Bahl, Self-induced Dirac boundary state and digitization in a nonlinear resonator chain, *Phys. Rev. Lett.* **129**, 135501 (2022).
- [52] D. Zhou, D. Z. Rocklin, M. Leamy, and Y. Yao, Topological invariant and anomalous edge modes of strongly nonlinear systems, *Nat. Commun.* **13**, 3379 (2022).
- [53] B. G.-g. Chen, N. Upadhyaya, and V. Vitelli, Nonlinear conduction via solitons in a topological mechanical insulator, *Proc. Natl. Acad. Sci. USA* **111**, 13004 (2014).
- [54] Y. Hadad, V. Vitelli, and A. Alu, Solitons and propagating domain Walls in topological resonator arrays, *ACS Photon.* **4**, 1974 (2017).
- [55] A. N. Poddubny and D. A. Smirnova, Ring Dirac solitons in nonlinear topological systems, *Phys. Rev. A* **98**, 013827 (2018).
- [56] F. Ma, Z. Tang, X. Shi, Y. Wu, J. Yang, D. Zhou, Y. Yao, and F. Li, Nonlinear topological mechanics in elliptically geared isostatic metamaterials, *Phys. Rev. Lett.* **131**, 046101 (2023).
- [57] F. Zangeneh-Nejad and R. Fleury, Nonlinear second-order topological insulators, *Phys. Rev. Lett.* **123**, 053902 (2019).
- [58] Y.-L. Tao, N. Dai, Y.-B. Yang, Q.-B. Zeng, and Y. Xu, Hinge solitons in three-dimensional second-order topological insulators, *New J. Phys.* **22**, 103058 (2020).
- [59] Y. Zhang, Y. Kartashov, L. Torner, Y. Li, and A. Ferrando, Nonlinear higher-order polariton topological insulator, *Opt. Lett.* **45**, 4710 (2020).
- [60] M. S. Kirsch, Y. Zhang, M. Kremer, L. J. Maczewsky, S. K. Ivanov, Y. V. Kartashov, L. Torner, D. Bauer, A. Szameit, and M. Heinrich, Nonlinear second-order photonic topological insulators, *Nat. Phys.* **17**, 995 (2021).
- [61] V. O. Kompanets, H. Zhong, Y. Zhang, Y. V. Kartashov, Y. Li, S. A. Zhuravitskii, N. N. Skryabin, I. V. Dyakonov, A. A. Kalinkin, S. P. Kulik *et al.*, Observation of nonlinear fractal higher-order topological insulator, [arXiv:2402.01979](https://arxiv.org/abs/2402.01979).
- [62] M. Ezawa, Nonlinearity-induced transition in the nonlinear Su-Schrieffer-Heeger model and a nonlinear higher-order topological system, *Phys. Rev. B* **104**, 235420 (2021).
- [63] J. Yi and C. Chen, Delocalization and higher-order topology in a nonlinear elastic lattice, *New J. Phys.* **26**, 063004 (2024).
- [64] F. Allein, A. Anastasiadis, R. Chaunsali, I. Frankel, N. Boechler, F. K. Diakonos, and G. Theocharis, Strain topological metamaterials and revealing hidden topology in higher-order coordinates, *Nat. Commun.* **14**, 6633 (2023).
- [65] A. L. Vanel, O. Schnitzer, and R. V. Craster, Asymptotic network models of subwavelength metamaterials formed by closely packed photonic and phononic crystals, *Europhys. Lett.* **119**, 64002 (2017).
- [66] S. Palmer, Y. Ignatov, R. V. Craster, and M. Makwana, Asymptotically exact photonic approximations of chiral symmetric topological tight-binding models, *New J. Phys.* **24**, 053020 (2022).
- [67] C. H. Lee, S. Imhof, C. Berger, F. Bayer, J. Brehm, L. W. Molenkamp, T. Kiessling, and R. Thomale, Topoelectrical circuits, *Commun. Phys.* **1**, 39 (2018).
- [68] N. Lazarides and G. Tsironis, Superconducting metamaterials, *Phys. Rep.* **752**, 1 (2018).
- [69] M. Remoissenet, *Waves Called Solitons: Concepts and Experiments* (Springer Science & Business Media, New York, 2013).
- [70] R. W. Boyd, A. L. Gaeta, and E. Giese, Nonlinear optics, in *Springer Handbook of Atomic, Molecular, and Optical Physics* (Springer, Berlin, 2008), pp. 1097–1110.
- [71] K. J. H. Law, A. Saxena, P. G. Kevrekidis, and A. R. Bishop, Localized structures in Kagome lattices, *Phys. Rev. A* **79**, 053818 (2009).
- [72] X. Zhu, H. Wang, and L.-X. Zheng, Defect solitons in Kagome optical lattices, *Opt. Express* **18**, 20786 (2010).
- [73] R. A. Vicencio and M. Johansson, Discrete flat-band solitons in the Kagome lattice, *Phys. Rev. A* **87**, 061803(R) (2013).
- [74] M. I. Molina, Localized modes in nonlinear photonic Kagome nanoribbons, *Phys. Lett. A* **376**, 3458 (2012).
- [75] M. Ezawa, Higher-order topological insulators and semimetals on the breathing Kagome and pyrochlore lattices, *Phys. Rev. Lett.* **120**, 026801 (2018).
- [76] H. Xue, Y. Yang, F. Gao, Y. Chong, and B. Zhang, Acoustic higher-order topological insulator on a Kagome lattice, *Nat. Mater.* **18**, 108 (2019).
- [77] X. Ni, M. Weiner, A. Alu, and A. B. Khanikaev, Observation of higher-order topological acoustic states protected by generalized chiral symmetry, *Nat. Mater.* **18**, 113 (2019).
- [78] S. Kempkes, M. R. Slot, J. J. van Den Broeke, P. Capiod, W. A. Benalcazar, D. Vanmaekelbergh, D. Bercioux, I. Swart, and C. M. Smith, Robust zero-energy modes in an electronic higher-order topological insulator, *Nat. Mater.* **18**, 1292 (2019).
- [79] Q. Wu, H. Chen, X. Li, and G. Huang, In-plane second-order topologically protected states in elastic Kagome lattices, *Phys. Rev. Appl.* **14**, 014084 (2020).
- [80] Z. Wang and Q. Wei, An elastic higher-order topological insulator based on Kagome phononic crystals, *J. Appl. Phys.* **129**, 035102 (2021).
- [81] M. A. J. Herrera, S. N. Kempkes, M. B. de Paz, A. García-Etxarri, I. Swart, C. M. Smith, and D. Bercioux, Corner modes of the breathing Kagome lattice: Origin and robustness, *Phys. Rev. B* **105**, 085411 (2022).
- [82] G. Duan, S. Zheng, Z.-K. Lin, J. Jiao, J. Liu, Z. Jiang, and B. Xia, Numerical and experimental investigation of second-order mechanical topological insulators, *J. Mech. Phys. Solids* **174**, 105251 (2023).
- [83] L. Fang and M. J. Leamy, Dispersion morphing in stretchable rotator lattices, *Phys. Rev. Appl.* **20**, 034057 (2023).
- [84] J. Marín and S. Aubry, Finite size effects on instabilities of discrete breathers, *Physica D* **119**, 163 (1998).
- [85] P. Li, R. Li, and C. Dai, Existence, symmetry breaking bifurcation and stability of two-dimensional optical solitons supported by fractional diffraction, *Opt. Express* **29**, 3193 (2021).
- [86] B. M. Manda, R. Carretero-González, P. G. Kevrekidis, and V. Achilleos, Skin modes in a nonlinear Hatano-Nelson model, *Phys. Rev. B* **109**, 094308 (2024).
- [87] M. Ezawa, Nonlinear non-Hermitian higher-order topological laser, *Phys. Rev. Res.* **4**, 013195 (2022).

- [88] B. Krauskopf, H. M. Osinga, and J. Galán-Vioque, *Numerical Continuation Methods for Dynamical Systems* (Springer, Berlin, 2007), Vol. 2.
- [89] C. Padmanabhan and R. Singh, Analysis of periodically excited non-linear systems by a parametric continuation technique, *J. Sound Vib.* **184**, 35 (1995).
- [90] C. Hoogeboom, G. Theocharis, and P. G. Kevrekidis, Discrete breathers at the interface between a diatomic and a monoatomic granular chain, *Phys. Rev. E* **82**, 061303 (2010).
- [91] M. Chung, Y.-L. Cheon, and H. Qin, Linear beam stability in periodic focusing systems: Krein signature and band structure, *Nucl. Instrum. Methods Phys. Res., A* **962**, 163708 (2020).
- [92] S. Aubry, Discrete breathers: localization and transfer of energy in discrete hamiltonian nonlinear systems, *Physica D* **216**, 1 (2006).
- [93] S. Flach and A. V. Gorbach, Discrete breathers—advances in theory and applications, *Phys. Rep.* **467**, 1 (2008).